Structure of Hydroxylated Galactocerebrosides from Myelin at the Air-Water Interface

Karlheinz Graf,*† Hubert Baltes,‡ Heiko Ahrens,§ Christiane A. Helm,§ and Cynthia A. Husted*
*Neuroscience Research Institute, Biological Sciences 2, University of California, Santa Barbara, CA 93106-5060 USA, †Universität-Gesamthochschule Siegen, Institut für Physikalische Chemie II, 57068 Siegen, Germany, ‡Max-Planck-Institut für Kolloid- und Grenzflächenforschung, 14476 Golm, Germany, and §Institut für Angewandte Physik, Ernst-Moritz-Arndt-Universität Greifswald, 17487 Greifswald, Germany

ABSTRACT Hydroxy-galactocerebrosides (mixed chain length, constituent of myelin membranes) from bovine brain are investigated as monolayers at the air-water interface with isotherms, fluorescence microscopy, x-ray reflectivity and grazing incidence diffraction. With grazing incidence diffraction a monoclinic tilted chain lattice is found in the condensed phase. According to x-ray reflectivity, the longest chains protrude above the chain lattice and roughen the lipid/air interface. On compressing the chain lattice, the correlation length increases by ~65%; obviously, the sugar headgroups are flexible enough to allow for lattice deformation. With fluorescence experiments, small coexisting fluid and ordered domains are observed, and there is lipid dissolution into the subphase as well. The dissolved hydroxy-galactocerebroside molecules reenter on monolayer expansion. The electron density profiles derived from x-ray reflectometry (coherent superposition) show that the chain-ordering transition causes the molecules to grow into the subphase.

INTRODUCTION

Galactocerebrosides (GalC) are double-chained glycosphingolipids with one galactosyl headgroup. There exist different types of GalC, including neutral hydroxy- and nonhydroxy GalC (HFA and NFA) and the negatively charged sulfatides GalC (sGalC). They have been found in significant concentrations only in the outer leaflet of myelin (Alberts et al., 1983). Myelin acts as a multilamellar insulator around brain axons and is expressed by oligodendrocytes in the central nervous system (Stryer, 1988).

Several biochemical functions for the mixtures of GalC have been suggested (Coetzee et al., 1998). From studies with antibodies to GalC it was concluded that these lipids participate in the opening of Ca^{2+} channels in the oligodendrocytes (Dyer and Benjamins, 1990, 1991). Additionally, they might serve as a mediator for cell-cell recognition and as a receptor for viral and bacteria toxins. It was suggested that because of its high acyl chain order-disorder transition temperature, GalC might increase order in myelin, thus decreasing permeability to ions and facilitating saltatory conduction (Curatolo, 1986; Bosio et al., 1998). Furthermore, it was suggested that GalC and sGalC together with cholesterol and integral or peripheral proteins form rafts which could interact with complementary structures of an apposing membrane (Simons and Ikonen, 1997; Bosio et al., 1998). Recently, a strong interaction across apposed bilayers between GalC and sGalC mediated by Ca^{2+}-ions was found (Boggs et al., 2000) where the interaction among the HFA species seems to be the strongest (Koshy et al., 1999). These interactions were accompanied by dehydration of the headgroups and the interface region between the bilayers.

Alterations in the amount and/or the molecular shape of the GalC in myelin might therefore affect the structure of myelin in the brain and spinal cord, which could lead to serious disorders such as multiple sclerosis. The spiral arrangement of the myelin lipid bilayer was shown to form a more favorable vesicular shape in acute multiple sclerosis (Genain et al., 1999). Measurements on NFA alone have shown that this lipid prefers to aggregate into nanotubes with highly curved structure (Ohler et al., 2001). Obviously, these shape alterations and the interaction of the sugar headgroup with different targets are crucial for a better understanding of multiple sclerosis and other disorders of myelin.

Here, we concentrate on HFA, which in contrast to NFA has an additional hydroxy group in one of the lipid chains thus allowing for additional hydrogen bonds (Pascher and Sundell, 1977; Lee et al., 1986). We investigated HFA as a monolayer on the water surface to probe the lateral interactions as well as the mechanisms leading to monolayer destabilization.

MATERIALS AND METHODS

Materials

HFA (Type I, 98% α-hydroxy fatty acids) was purchased from Sigma (St. Louis, MO). It is isolated from bovine brain and represents a mixture of different chain lengths (Fig. 1). According to a gas-liquid chromatography analysis (Johnston and Chapman, 1988), the length of the acyl chain varies between 16 and 26 carbon atoms. The most abundant chain lengths are 18 (32%) and 24 (38.5%), and the average molecular weight is 801. All data presented here (lengths, average electron density, molecular weight) are based on the chain-length distribution presented there, which we are assuming has not changed. Its correctness is supported by the fact that our

Submitted July 18, 2001, and accepted for publication October 12, 2001.
Address reprint requests to: Dr. C. A. Helm, Institut für Angewandte Physik, Ernst-Moritz-Arndt-Universität Greifswald, Friedrich-Ludwig-Jahn-Straße16, 17487 Greifswald, Germany. Tel.: 49-3834-86-4710; Fax: 49-3834-86-4712; E-mail: christiane.helm@physik.uni-greifswald.de.

0006-3495/02/02/896/12 $2.00

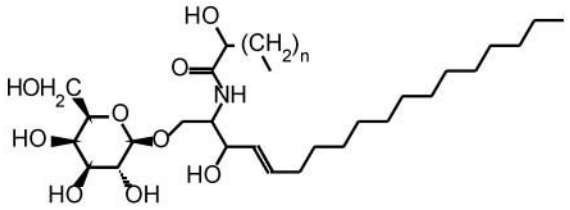

FIGURE 1 Molecular structure of HFA from bovine brain. The acyl chain length varies from 18 to 24 carbon atoms ($15 \leq n \leq 21$), whereas the length of the alkyl chain is constant.

results were reproducible for several HFA charges acquired in a range of 2 years. To get an idea of how far-reaching the changes in the chain length composition might be, we recalculated the average molecular weight and the average number of electrons per molecule on the base of another composition analysis of HFA from total brain extract (Sastry, 1985). There, much fewer acyl chains with 18 carbon atoms occurred (16% instead of 32%) and chains with longer chains (>24 carbon atoms) were present in larger amounts. The error in the recalculated values is 2%, which does not affect our interpretation at all.

The HFA was dissolved in a mixture of hexane:chloroform:ethanol (11:5:4 v/v) in a concentration of 0.4–0.6mM. The solvents were purchased from Merck (Darmstadt, Germany) and the solutions were kept below 0°C in a freezer until use. For fluorescence microscopy a dye-labeled lipid was added to a solution of HFA (1.2 mM) in a concentration of 1 Mol-% (dye: 1-palmitoyl-2-[6-[(7-nitro-2–1,3-benzoxadiazol-4-yl)amino]caproyl]-sn-glycero-3-phosphocholine from Avanti Polar Lipids, Alabaster, AL). The absorption maximum is at 460 nm, the maximum of the emission light at 534 nm.

Langmuir trough and fluorescence microscopy

The fluorescence experiments were carried out on a homemade poly(tetrafluorethylene) (Teflon, DuPont, Wilmington, DE) Langmuir trough (A_{min} = 17.9 cm^2, A_{max} = 112 cm^2, compression ratio = 1:6) under air at 30°C. Pure water (Millipore, Bedford, ME, $\rho \leq 18$ M$\Omega \cdot$ cm) served as a subphase. The fluorescence images were recorded without any further filtering or frame averaging with a videocassette recorder, controlled by external monitoring.

X-ray reflectometry

The x-ray reflectometry experiments at the air-water surface were carried out with the Mainz x-ray reflectometer which consists of a Langmuir trough as in the fluorescence microscopy (300 × 160 mm^2 size, compression ratio 1:5.5) and a homemade θ/θ x-ray setup described in detail elsewhere (Baltes et al., 1996). This setup allows for investigation of thin organic films at the air-water interface at different molecular areas, providing the electron density perpendicular to the water surface. The trough is mounted in a gas-tight enclosure with x-ray transparent Capton windows sitting on an active vibration-attenuation table.

For x-ray experiments a conventional Cu anode (λ = 1.54 Å, 40 kV, 55 mA) with a line focus was used as a source. A good angular resolution is achieved by two sets of slits (two 400 μm slits and two 200 μm slits before and after the trough) and a graphite secondary monochromator in front of the NaI detector. The distance between detector and source is 1.5 m leading to an incident intensity of $\sim 1 \times 10^7$ counts/s. The transversal coherence length of the x-ray beam is 300 nm, leading to a horizontal coherence length on the sample of at least 2.5 μm (that value was calculated for incident angles of 5°) (Salditt et al., 1994).

The HFA solution was spread onto pure Millipore water after equilibration of the subphase at 30°C. A time of 10 min was considered to be sufficient to evaporate the solvents. To minimize water convection and mechanical drifts during data acquisition, the room was also heated up to 30°C.

After spreading, the film was precompressed to 50 mN/m with 1.0 Å^2/molecule/min and then expanded completely to achieve an equilibrium film. Afterwards, the thin lipid film was compressed slowly to different pressure/area values (compressing speed 0.5–1.5 Å^2/molecule/min) without turning on the x-ray source to minimize radiation damage. A relaxation time of 30 min was allowed at constant areas and the pressure relaxation was recorded. After performing the x-ray measurements at different π/A values during compression and expansion (2–3 h/point) the reproducibility of the isotherm and the reflectograms was verified.

The x-ray data were background-subtracted and normalized to the Fresnel reflectivity R_F (convoluted with the resolution function) of a sharp air-water interface. The deviation of the refractive index from 1 is very small for x-ray radiation, thus dynamic effects (i.e., multiple scattering can be neglected for angles larger than two or three critical angles $Q_{z,c}(H_2O)$ = 0.022 Å^{-1}). Therefore, the measured and normalized reflectivity R/R_F is given in a kinematic approximation by the so-called master formula (Als-Nielsen, 1986)

$$\frac{R}{R_F} = \frac{1}{\rho_w^2} \left| \int \rho'(z) e^{iQ_z z} dz \right|^2 \quad (1)$$

where ρ_w is the electron density of the bulk phase ($\rho_w(H_2O)$ = 0.333 e$^-$/Å^3), $\rho(z)$ the gradient of the electron density along the surface normal, z, and Q_z the wave vector transfer in z-direction ($Q_z = 4\pi/\lambda \cdot \sin\theta$ with λ the wave length and θ the angle vs. the water surface). For quantitative comparisons between models and data, calculations including refraction and multiple scattering were performed with the matrix algorithm (Parratt, 1954; Asmussen and Riegler, 1996).

Modeling of the measured reflectometry requires comparing a calculated electron density distribution of a reasonable simplified model with R/R_F. A general approach is to divide the electron density into i slabs (so-called "boxes") of a certain length or layer thickness d_i and electron density ρ_i, which should be identified with characteristic structural features of the molecules. Typically, amphiphilic molecules are divided into two boxes, one for the hydrophilic headgroup and one for the hydrophobic chain regime. Moreover, the interface between the various slabs are smeared by a roughness σ (Helm et al., 1987a; Als-Nielsen, 1986). From the electron density in each slab the number of electrons $N_{e,i}$ per slab can be calculated from

$$N_{e,i} = \rho_i \cdot a \cdot d_i \quad (2)$$

with a being the molecular area (Helm et al., 1991). Generally, the sum of the electrons in all slabs differs from the number of electrons from the structural formula. Usually, excess electrons are attributed to water molecules within the polar headgroup (10 electrons/water molecule) and a loss of electrons hints at a loss of molecules into the subphase or the air.

In general, various models can be used to obtain the same electron density profile (Baltes et al., 1996; Pershan, 1994) and reflectivity curves. The best agreement of the model function with the data is determined by least-square methods. As a further cross-check, least structured electron density profiles were calculated with model independent fits on the base of a method developed by Pedersen (1992) and Pedersen and Hamley (1994). The general approach is to keep the number of slabs and the number of parameters describing the thin film as low as possible to avoid ambiguity of the interpretation. Unfortunately, the parameterization of an electron density profile gets ambiguous when one slab thickness d is smaller than the roughness of the adjacent interfaces (i.e., $d \leq 2\sigma$). In that case an unphysical increase in the electron density ρ of that slab is compensated by a decrease in its thickness, resulting in a series of (d,ρ) pairs with nearly indistinguishable density profiles. This problem occurs especially with the

lipid headgroup; to avoid unphysical results, we set the corresponding layer thickness to physically reasonable values. Unless indicated otherwise, all interfaces are smeared by the same roughness σ, which is of the order of the dynamic roughness of the water surface (Pershan, 1994).

Moreover, we used x-ray reflectometry on laterally inhomogeneous phases. Lateral inhomogeneities (phase separation) of the monolayer affect the reflected intensities in two different ways, depending on the length scale of the inhomogeneities i.e., the domain size (Helm et al., 1991). If the domain size is smaller than the lateral coherence length, then x-rays scattered in different phases interfere with one another, which is described by an average electron density. Here, the resulting electron density $\rho_{res}(z)$ is the coherent superposition of the electron density of the single domains

$$\rho_{res}(z) = \alpha \cdot \rho_1(z) + (1 - \alpha) \cdot \rho_2(z) \quad (3)$$

where the different phases are weighted with their respective area fractions, α, leading to so-called isosbestic points (i.e., points independent of α) in the electron density profile, not in the reflectivity. The reflectivity of the film is then calculated with this average electron density.

If the domain size is larger than the coherence length, the respective reflectivities of the phases are summed up, again weighted with their area fractions

$$R_{res}(Q_z) = \alpha \cdot R_1(Q_z) + (1 - \alpha) \cdot R_2(Q_z) \quad (4)$$

leading to isosbestic points in the reflection curve.

Synchrotron grazing incidence diffraction (GID)

GID was carried out at the beamline BW1 in HASYLAB, the Hamburg Synchrotron laboratory (Germany) at room temperature in a set-up described earlier (Kjaer et al., 1987; Als-Nielsen and Kjaer, 1989). Generally, condensed lipids at the air-water-interface order in a more or less distorted hexagonal two-dimensional (2-D) lattice, where the third Bragg condition in the (vertical) z-direction is relaxed, leading to a 2-D ordered lattice of so-called Bragg rods in reciprocal space. The positional order in 2-D hexatic or liquid crystalline systems decays exponentially (Helm et al., 1987b; Nelson and Halperin, 1979), resulting in a Lorentzian lineshape in Q_{xy} of the diffraction peaks (in a hexatic lattice the decay is algebraic, but that can not be resolved; therefore, we describe the peaks as Lorentzians). The peak width $\Delta(Q_{xy})$ is the reciprocal of the correlation length, i.e., it describes the decay of the positional order.

The shape of the ordered scattering centers (generally the alkane chains in all *trans* conformation) can be described in a simplifying way as a cylinder of length 1. In direction of its axis, the Fourier transform of the cylinder, i.e., its molecular form factor is described by a slit-function, which can be approximated by a Gaussian with full width half maximum (FWHM)(Q_z) = 5.31/1. Because the cylinder radius is much smaller than its length l, the form factor of the cylinder is a disk in reciprocal space. If generally the cylinder is tilted from the water surface normal by a tilt angle t in a direction ψ with respect to the crystal axis, the disk in reciprocal space is rotated by the same angle ψ. Diffraction peaks arise at the cross-sections of the tilted disk with the Bragg rods of the 2-D lattice. The molecular tilt is generally accompanied by a distortion of the hexagonal lattice with its triple-degenerated peak. For a tilted lattice, two or three peaks at different positions in the Q_{xy}, Q_z plane are expected, with the constraint that the greatest Q_z value is the sum of the other two Q_z values. For example, if the chains are tilted toward the nearest neighbors, the lattice is orthorhombic-distorted with one peak at $Q_{z1} = 0$ and a double peak at $Q_{z2} > 0$ and $Q_{xy2} < Q_{xy1}$.

Because lipid films form a 2-D powder, GID experiments at the air/water interface are akin to a Debye-Scherrer setup, and no restriction of sample orientation with respect to the beam has to be considered.

RESULTS AND DISCUSSION

Isotherms and fluorescence microscopy

Fig. 2 shows the Isotherms of HFA at 20°C and 30°C on pure water, together with fluorescence microscopy images taken at the higher temperature. At 20°C, the onset of the pressure increase occurs at 44 Å^2/molecule. At 39 Å^2 and 8 mN/m an abrupt change of slope occurs, and beyond that kink the pressure increase is steep. At the higher temperature, the pressure rises smoothly at a much larger area per molecule ($\approx$ 70 Å^2 at second compression). Again, at ~40 Å^2 the isotherm becomes very steep. During the first compression the isotherm is unstructured as presented in the literature (Ries, 1982). The minimum molecular area of 35 Å^2/molecule is much lower than expected from space-filling models for double-chained amphiphiles, 40 Å^2/molecule for two nontilted chains in the all-*trans* conformation. (The 52 Å^2/molecule for lipids with a sugar group as deduced from crystal data (Pascher and Sundell, 1977) shows that the crystal data are irrelevant in this context.). Therefore, we have to conclude that the HFA film tends to form multilayers or micelles leading to loss of material in the surface plane. The molecules are reentering the smooth water surface after expansion to the maximum area as seen by the reversibility of the isotherm. The fluorescence images show that the film is largely inhomogeneous with a broad distribution of domain sizes ~5 μm. Although the fluorescence microscopy results will be discussed separately, we can expect that the x-ray reflectivity signals will be mostly coherently superimposed, because the lateral coherence length is 2.5 μm.

X-ray reflectometry: homogeneous phases

During the second compression we measured the x-ray reflectograms at different molecular areas over a period of ~15 h. The isotherm for the second compression is shifted to larger areas, shows a pressure relaxation of 4 mN/m after barrier stops, and exhibits a slight kink at 20 mN/m between 40 and 42 Å^2/molecule (cf. the isotherm in the inset of Fig. 3). We observe the same changes but less pronounced in a film compressed extremely slowly (15 h) under the same conditions but without exposure to x-ray radiation. This might be attributable to the presence of unsaturated lipid chains ($\approx$ 5%), which are more sensitive to damage than saturated ones. This is supported by the observation that the isotherm is slightly shifted (2–3 Å^2) to a higher molecular area when measured under air instead of helium. Nevertheless, the reflectograms remain the same within the confidence limits measured for different samples, different film histories, or under different air conditions.

The reflectograms (*points*) measured at five different molecular areas and the fits (*lines*) are shown in Fig. 3, the inset showing the molecular areas at which the x-ray mea-

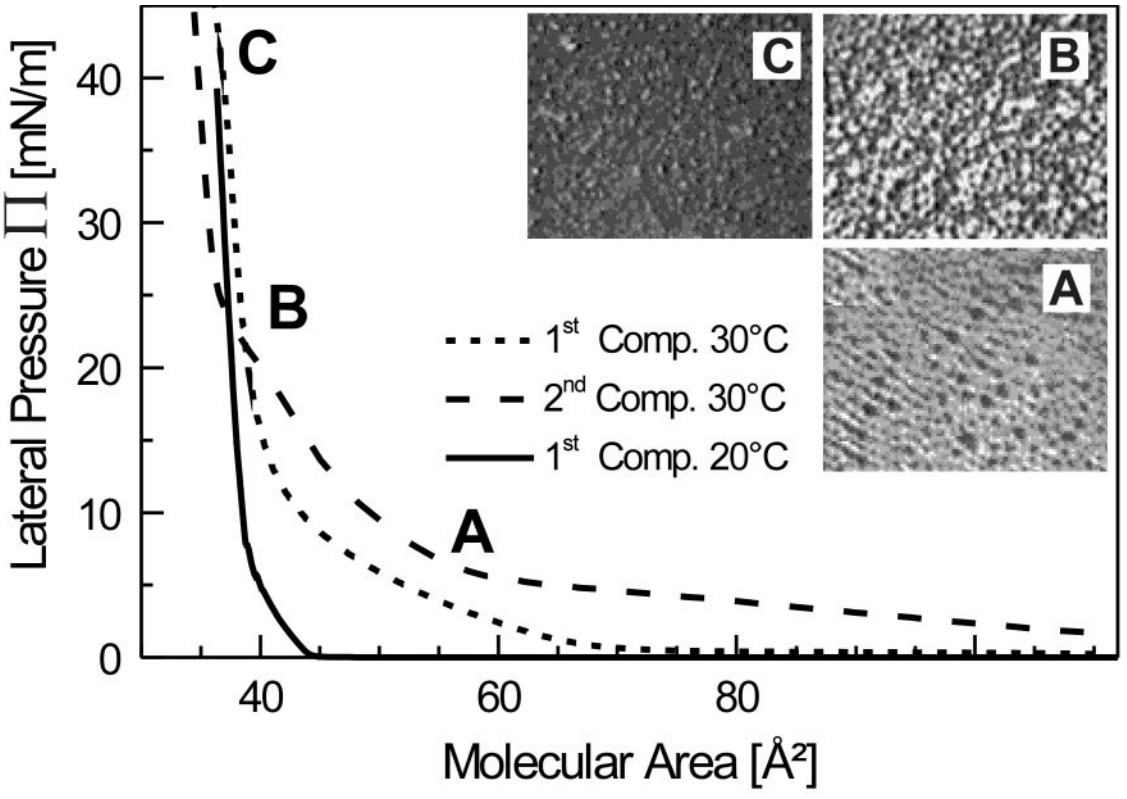

FIGURE 2 Isotherm of HFA on pure water at 20° and 30°C. The straight line is the 20°C isotherm. The dotted line is the 30°C isotherm for the first compression after spreading and a waiting time of 15 min. The dashed line corresponds to the 30°C equilibrium isotherm from the second compression during which the x-ray measurements were performed. At *A* and *B* fluorescence microscopy images show a phase separation within the HFA film similar to those of other lipids (image size 114 × 100 μm^2). At *C* the film seems to have less contrast with remaining dark domains and with a few bright spots.

surements were performed. The top reflectograms (*a*–*c*) exhibit one broad minimum at ~0.25 $Å^{-1}$, whereas in the curves (*d*, *e*) obtained at high pressures two minima are found. The first minimum of *d*, *e* appears at 0.18 $Å^{-1}$, the second one at 0.4 $Å^{-1}$ being not simply a higher order of the first one. Inspecting reflectogram *e* in detail, the first minimum is one order of magnitude deeper than in the other curves and the intensity of the third maximum at ~0.45 $Å^{-1}$ is strongly diminished with respect to the second one. Comparing the reflectograms *a*, *b*, and *c*, one observes a flattening in the curve *c* behind 0.3 $Å^{-1}$.

Generally, the shift to lower Q_z in the first minimum upon compression from curve *a* to *e* is an indication of increasing film thickness. An initial simple estimate ($Q_{z,min} \cdot d = \pi$) of the lengths from the position of the minima shows that the thickness increases from 12 to 18 Å (from the first minimum) and there is a constant molecular thickness of ~8 Å (from the second one). If one compares these lengths with the molecular structure shown in Fig. 1, one might identify the longer part with the alkyl/acyl chains of HFA and the shorter one with the polar headgroup consisting mainly of the sugar group. The overall film thickness of 20 to 26 Å is consistent with a monolayer, and there is no obvious indication of material loss that the isotherm suggests for *e*.

The pronounced change in the reflectograms from *b* to *d* and the flattening in *c* indicate a more complex structure within the film. This obviously happens between 40 and 80 $Å^2$/molecule. The increased depth of the first minimum in *e* compared with *d* is a hint for a more homogeneous film. The diminished intensity of the third maximum in the same reflectogram might be explained by an increased roughness in the monolayer.

To learn more about the molecular structure of the HFA monolayer, we applied fits to the reflectograms and extracted the corresponding electron density profiles (Fig. 4 *a*). Various models were tried. The electron densities are so complex that more parameters are necessary than we can assign unambiguously. For now, we just discuss the density profiles obtained (The fit details are discussed in the Appendix). Whereas with other models the absolute values of the parameters are slightly shifted, the trends remained the same.

Going from air to water with increasing *z* (chain/air interface: $z = 0$), the electron density profiles exhibit two major features: an oblique step at ~0.30 electrons/$Å^3$ and a maximum with a height between 0.38 and 0.44 electrons/$Å^3$ (water: 0.333 electrons/$Å^3$). The former is attributed to the chain slab, the latter to the headgroup. As in the reflecto-

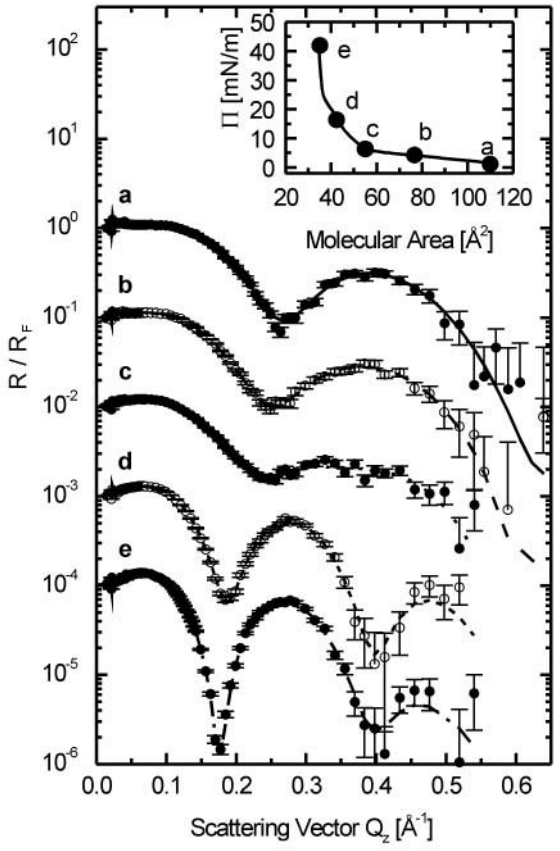

FIGURE 3 Specular x-ray reflectograms on a film of HFA on water at 30°C. The reflectograms were measured at points *a–e* of the isotherm during the second compression (*inset*: equilibrium isotherm from Fig. 2). After each compression step (compressing speed: 0.5–1.5 Å^2/molecule/min), the film was allowed to relax for 30 min before the x-ray measurement was done (2–3 h per curve). The data were background corrected and normalized to the Fresnel reflectivity of an ideally smooth water surface. The lines represent fits according to the model described in the Appendix. With other models equally good fits could be obtained.

grams, two groups of electron density profiles can be distinguished. In *a* to *c* the chain slab is short (~14 Å) and the headgroup electron density is smaller (~0.39 electrons/Å^3) and occurs at lower *z*. In *d* and *e* the chain and headgroup slabs are thicker and the latter exhibits an electron density larger than 0.4 electrons/Å^3. The film thickening, the additional steps, and the asymmetric broadening can be seen in the derivative $d\rho/dz$ more precisely (Fig. 4 *b*).

Looking closer to the electron density profiles *b*, *c*, and *d*, one finds that the monolayer thickening occurs discontinuously. Actually, the headgroup seems to disappear at $z \approx 18$ Å and to reappear at $z \approx 27$ Å. We find an asymmetric broadening of the respective slabs (*arrows*). The same features can be recognized when considering the derivative $d\rho/dz$ (cf. Fig. 4 *b*). The distances between the extrema as denoted in the plot represent the thicknesses of the headgroup and the chain layer d_h and d_c, respectively. The distances as obtained from the derivates are plotted in Fig. 4 *c*. One finds basically two different sets of thicknesses, each of them basically constant. Whereas the headgroup thickness changes only slightly (8.3 to 9.4 Å), the chain thickness changes dramatically (14.3 to 22.6 Å). Tentatively, the different profiles can be attributed to a fluid and a condensed phase, which coexist in the range between *b* and *d*. To verify this idea, it is necessary to discuss the electron densities and the results obtained from other methods.

However, already this simple analysis demonstrates that the HFA reflectograms are typical for a monolayer: a chain and a headgroup slab can be recognized. The maximum headgroup electron density is 0.44 electrons/Å^3. A value of 0.5 electrons/Å^3 would indicate a sugar crystal (e.g., ρ(glucose) = 1.56 g/cm^3 $\equiv$ 0.5 electrons/Å^3). Although the interfacial roughness is a big source of error, we can conclude that the HFA headgroups are very compressed. Also, the pronounced overall film thickening on compression from 22.6 to 32 Å is not unusual.

The thickness of the hydrophobic layer (22.6 Å) exceeds the one of the ordered alkyl chains as determined by GID (18.6 Å). Also, the hydrophobic/air interface is rougher than all other monolayer interfaces. The most likely picture for the hydrophobic slab is a condensed ordered chain layer with a few protruding disordered hydrocarbon chains on top. This structure is caused by the chain-length mismatch as sketched in Fig. 1.

Fortunately, the number of electrons within a monolayer is just the *z*-integrated electron density, multiplied with the mean molecular area. It is independent of any model assumptions. In Fig. 4 *d* the amount of electrons per HFA molecule is shown. Usually, a lipid molecule is hydrated and the excess electrons are attributed to water molecules in the headgroup (cf. Eq. 2). Indeed, in the most expanded state 30 water molecules per HFA molecule are found in the headgroup layer. However, at a molecular area of 50 Å^2/molecule, the electron number decreases below the dehydrate (441 electrons), to 380 electrons. This indicates a virtual electron loss of ~14%. Because some hydration is very likely, the onset of monolayer instability and dissolution of HFA molecules into the water occurs probably above 50 Å^2/molecule, possibly simultaneously with the formation of a condensed phase. The reversibly dissolved HFA molecules can not be found in the reflectivity curves. To find them, fluorescence microscopy experiments were performed.

Fluorescence microscopy: inhomogeneous phases

The fluorescence images of the HFA film show dark spots (∅ some μm) in a bright dye-enriched phase (*A* in Fig. 2). Upon compression to ~25 mN/m, the dark spots persist and the optical contrast increases (*B* in Fig. 2) whereas the

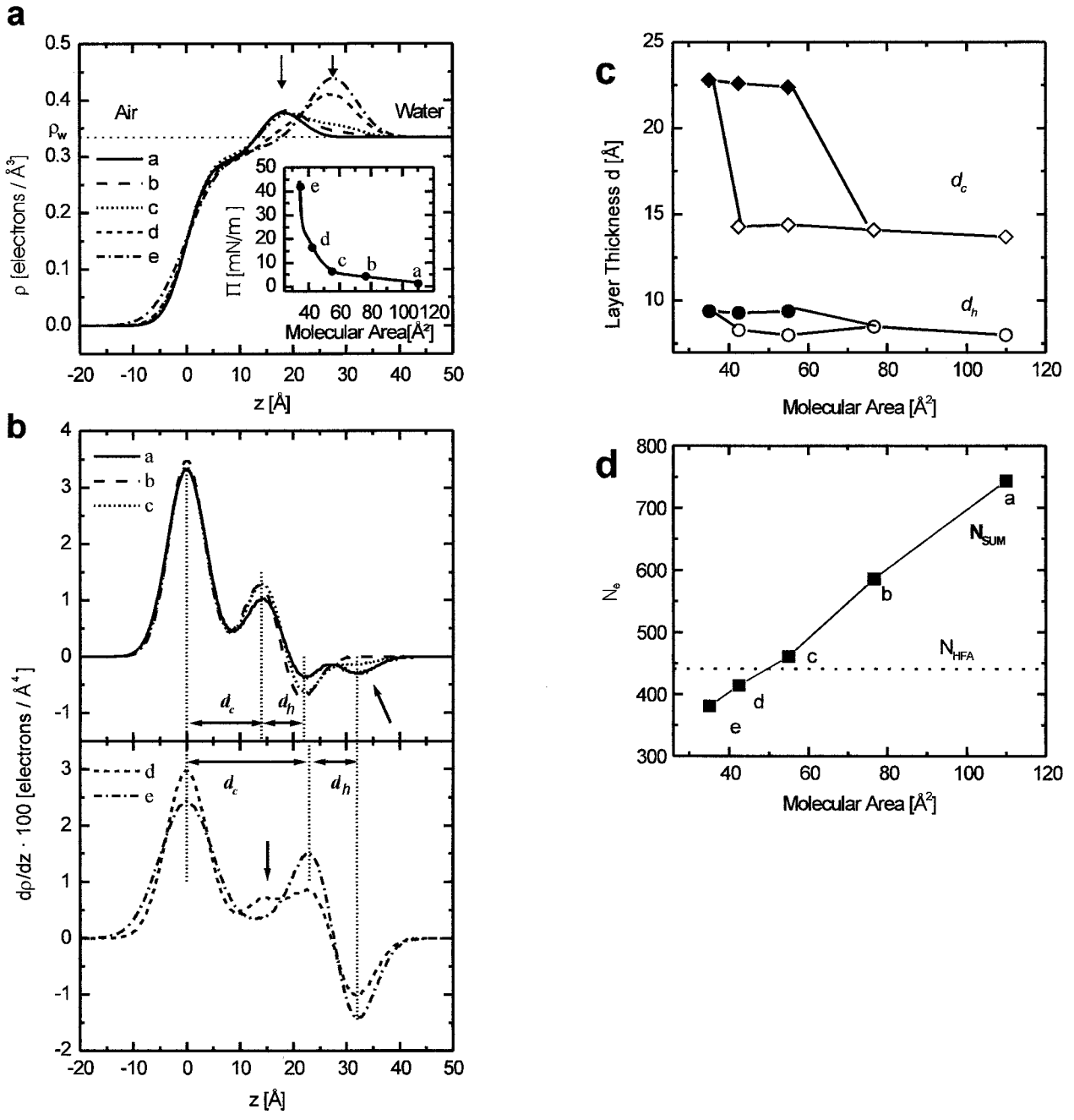

FIGURE 4 Electron density profiles and their derivatives for HFA on pure water at 30°C. (*a*) The profiles were obtained from slab models as described in the text. They represent the electron density perpendicular to the water surface in direction of the subphase ($z = 0$: film/air interface). (*b*) Derivative of the electron density with respect to z. This plot directly shows the thicknesses d_c and d_h of the headgroup and the chain layer as the distance between the extrema. Moreover, shifting maximum positions on increased surface pressure indicate changes in the layer thickness (*arrows*). For curves *b*, *c*, and *d*, additional extrema indicate phase coexistence. (*c*) d_c and d_h as calculated from (*b*). Open symbols indicate the fluid phase, solid symbols the condensed phase. (*d*) Number of electrons N_e vs. molecular area as determined from the isotherm. The dotted line indicates the 441 electrons attributed to the average dehydrated HFA molecule.

domains seem to be connected. Panels *A* and *B* both exhibit a distribution in domain size and shape of ~5 μm. Compression to 50 mN/m diminishes the contrast again with persisting bright spots (*C* in Fig. 2) and dark domains within a gray matrix. On increasing the lateral pressure from *A* to *B* to *C*, the film convection decreases indicating an increased film stiffness. Full expansion leads to the same morphology as in *A* with the dark spots still present. Please note that we were not able to expand the film further (to 110 Å^2/molecule).

The dark spots in *A* and *B* highlight monolayer inhomogeneity. A possible interpretation is a liquid-condensed phase (dark) in a liquid-expanded (bright) or gas matrix. The dark spots can not be in a gas phase because they would disappear upon compression to high pressures, which was not observed (Helm et al., 1987b).

The contrast enhancement from *A* to *B* might be created by further film condensation and thus an enrichment of dye between the condensing domains or just by the increased molecular density. A further lipid condensation possibly could occur between *b* and *d* without a pronounced coexistence plateau in the isotherm because a multicomponent mixture might increasingly shift the plateau to higher pressures with ongoing compression and thus smear it out (Miller and Möhwald, 1987). Additionally, experiments at 37°C show less ambiguous fluorescence images (not shown). HFA forms star-like domains in a brightly shining matrix beautifully demonstrating the coexistence of two different phases and the growth of a dark phase at the expense of the bright phase. At high compression (*C*) a homogeneous monolayer appears very dark because of quenching. However, the presence of bright spots at *C* indicates partial loss of material into the subphase or the air (Ding et al., 2001; Lipp et al., 1997). The lost material is obviously very close to the monolayer; otherwise it could not be observed with the fluorescence microscopy.

In contrast, the well structured curve *e* in x-ray reflectometry, measured at nearly the same pressure, indicates a homogeneous monolayer. Simulations and fits of the electron density profiles assuming partial multilayer formation (0–15%) show that the molecules rather tend to form diffuse micelles just beneath the monolayer instead of well ordered multilayers. A loss of molecules into the air can be excluded because the reflectivity highly depends on the difference of the electron density at the film interfaces, being at maximum for the air-film interface (Ibn-Elhaj et al., 1997; Ahrens et al., 1999). A loss of molecules ($\approx$ 13%) into the water subphase was already measured by the virtual loss of electrons as mentioned above. To better understand the condensed phase, GID measurements were performed.

GID at 20°C

The lack of the extended low-pressure regime at lower temperatures and comparison with other long chain lipids such as DSPE lead to the conclusion (Albrecht et al., 1978; Kenn et al., 1991) that HFA exists in the solid phase at room temperature. After spreading, tiny islands of condensed HFA are formed. At an area of 44 mN/m the corners of these islands or some fluid domains start to interact, leading to domain deformation but not to changes in local molecular ordering. A closed surface coverage is reached at 39 Å^2, followed by structural changes. Fig. 6 shows the diffraction peaks at pressures of 8, 15, 25, and 40 mN/m (corresponding to 38.6, 38, 37.1, and 36.3 Å^2). Three peaks with maxima at $Q_z > 0$ are attributable to tilted molecules in a monoclinic distorted hexagonal lattice with three different lattice spacings. On compression the peaks are shifted toward lower Q_z and higher Q_{xy} values, thereby getting closer to one another, indicating a decrease in tilt, lattice spacing, and the distortion from the hexagonal. At the highest pressure exists a nearly hexagonal lattice with nearly vertical oriented molecules.

To obtain more quantitative information, the data were fitted with a Lorentzian in Q_{xy} direction and a Gaussian in Q_z direction for each peak and a constant background. One constraint was introduced: for the peaks at high Q_z, the same width of peak in *xy* as well as in *z*-direction was used as for the one measured at low Q_Z.

The condensed chains of the HFA molecule are ordered in an monoclinic distorted hexagonal lattice with lattice constants of 4.970 (highly compressed) to 5.127 Å (most expanded) and 4.884 (highly compressed) to 4.904 Å (most expanded) enclosing an almost constant angle of 59.7 $\pm$ 0.1°. The molecules are 14° (highly compressed) to 20° (most expanded) tilted in a direction close to the longer crystal axis (deviation ψ = 5° (highly compressed) to 10° (most expanded)), that is close toward their nearest neighbor. The vertical correlation length, i.e., the thickness of the ordered chains remains constant within the error bar, 18.6($\pm$6)Å. This is a very reasonable value, with a distance of 1.25 Å along the molecular axis between adjacent carbon atoms and a thickness of 1.5 Å for the terminal methyl group, one obtains a number of 14.6 carbon atoms in the ordered chain, slightly more than the alkyl chain contains. Obviously, the thickness of the lipid chain lattice is limited by the alkyl chain (the hydrocarbon chain attached to the headgroup by a double bond), as the alkyl chain is shorter than the acyl chain, whatever the composition and length distribution is in detail. Therefore, there is little driving force for an accumulation of long-chain lipids in the condensed phase.

The area per two chains is greater than the area per molecule, probably because of loss of material as discussed earlier. On compression it is reduced from 43.6 Å^2 (below the kink in the isotherm at 8 mN/m) to 42 Å^2 (most compressed) with $\delta A(GID)/\delta A(Iso) < 1$, indicating stronger shrinking of unordered domains or loss of material. Yet, a larger compressibility (factor two) deduced from the isotherm than from diffraction is typical for phospholipid bilayers. It is attributed to lattice-defect annealing and domain rearrangement (Helm et al., 1987b, 1991; Möhwald et al., 1995); therefore, for HFA we can not take the difference in compressibilities as an indication of material loss.

The kink in the isotherm at 39 Å^2 and 8 mN/m is manifested in the behavior of all parameters characterizing the in-plane structure. At larger areas, they remain basically constant, indicating a coexistence of ordered domains with a gas phase. Beyond 8 mN/m, the domains are apparently compressed. The chain tilt *t* and the area per chain are especially affected, as

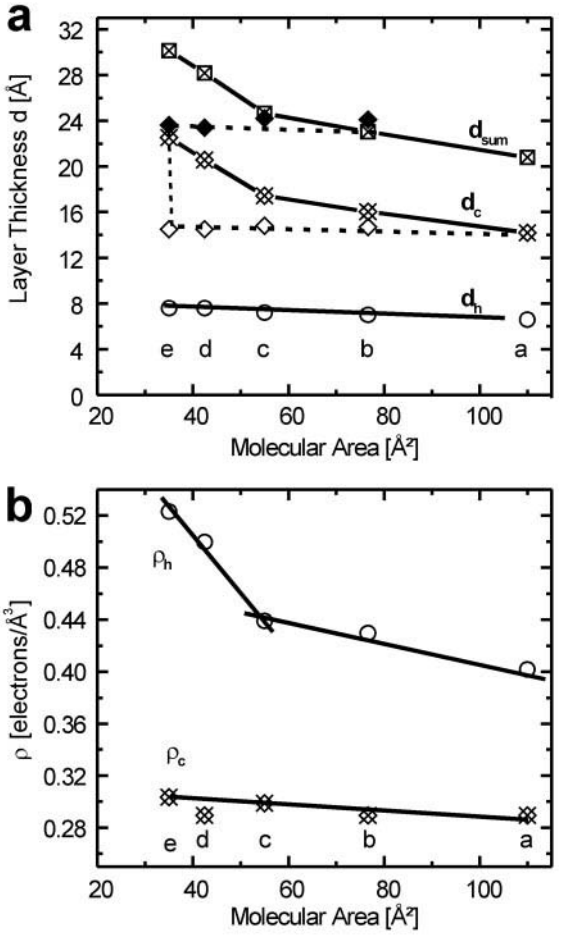

FIGURE 5 Layer thickness and electron density for HFA on pure water at 30°C. (*a*) The thicknesses d_c and d_h are the values taken from the domain model and deviate slightly from the distances of the extrema in Fig. 4 *b*. Open symbols indicate the fluid phase, solid symbols the condensed phase and symbols with stars average values valid for the whole film (connected by a *straight line*). Open and solid diamonds (connected by a *dashed line*) indicate the two different values obtained for the chain layer thickness (*b–e* only), which are attributable to coexisting domains of different thickness. (*b*) Average electron density for headgroup and chain layer.

shown in Fig. 6 *b*. Very intriguingly, the lateral correlation length in tilt direction jumps from 50 Å (pressures below 8 mN/m) to 80 Å (above 8 mN/m), i.e., 10–15 chain diameters. The behavior perpendicular to the tilt direction is different. Here the constant correlation length of 90 Å (below 8 mN/m) increases linearly on compression up to 150 Å. This behavior is highly unusual, very different from phospholipid or fatty acid monolayers (Möhwald et al., 1995; Kaganer et al., 1999). Within one condensed phase the correlation length is a constant, and the area per chain is almost a constant, too. This inflexibility is attributed to the headgroups, which frustrate the chain lattice, induce lattice defects, and hinder chain rotation or higher compression. It seems the headgroup influence is less pronounced for HFA. Also, it seems that HFA molecules dissolve reversibly from the monolayer. One may speculate

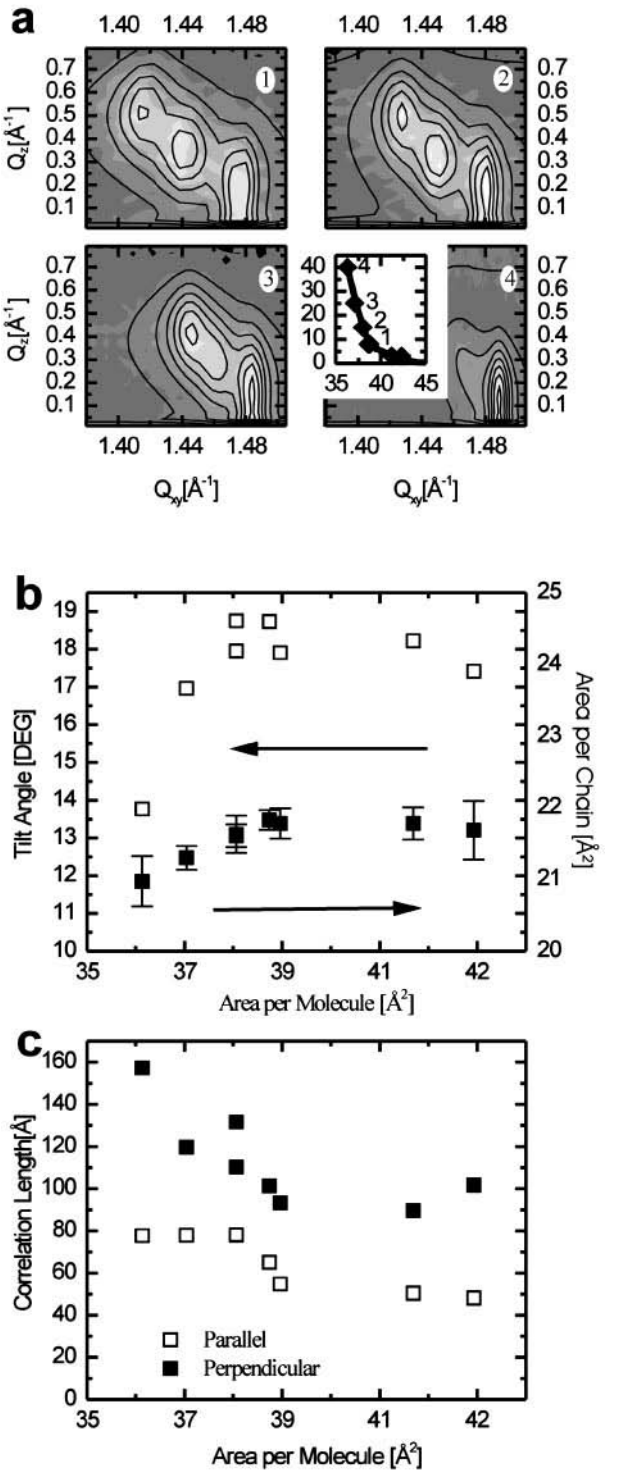

FIGURE 6 (*a*) In-plane GID scans performed along the isotherms at 8, 15, 25, and 40 mN/m (corresponding to molecular areas of 38.6, 38, 37.1, and 36.3 Å^2 as indicated in the isotherm in the insert). (*b*) The tilt angle (□) and the area per chain (■) as function of the mean molecular area. (*c*) The correlation length parallel (□) and perpendicular to the tilt direction (■) as function of the mean molecular area. Note that at 8 mN/m/39 Å^2 a kink is found in the isotherm; beyond this phase-transition, the domains obviously interact.

that the increase in correlation length on compression and the unusual high compressibility may be correlated to the higher mobility perpendicular to the monolayer. All these features point to an unusual low headgroup influence, possibly caused by an unusually small headgroup diameter, as well as the weak interaction between the sugar headgroups (Pincet et al., 2001; Lee et al., 1986).

X-ray reflectometry: inhomogeneous phases

It was already mentioned above that two sets of reflectograms were found: the curves *a* to *c* with one minimum and the more structured curves *d* and *e* with two minima. The main change occur between 40 and 80 $Å^2$/molecule and the electron density profiles *b* to *d* represent this change. The differentiation $d\rho/dz$ reveals most clearly that the profiles are a superposition of the profiles *a* and *e* which, in a first approach, might be considered as pure phases. This means that we *simultaneously* find two phases with a different thickness and *not* a monotonous increase in thickness with compression. This is a refinement of the results found in the fluorescence microscopy.

Yet, two problems need to be addressed: (1) Is coherent superposition really better than incoherent superposition? and (2) Examining Fig. 4 we see the condensed phase grows into the water with the same chain/air interface for both phases. However, in the commonly accepted model, one assumes that in a phase coexistence the chain/headgroup interface is a constant of the system and on chain condensation the chain/air interface is subject to an offset.

First, we describe our problems with incoherent superposition. When superposing the reflectograms *a* to *d* we do not observe an isosbestic point. Furthermore, the minima in the calculated reflectograms never match the measured curves, even for different values of the area fraction α of the fluid phase. For example, if one compares the intensities in the reflectograms at $Q_z = 0.3$ $Å^{-1}$ for the curves *a*, *c*, and *d*, we find that the intensity in *c* is so low that it never can be calculated by Eq. 4. Assuming incoherent superposition, we have to assume additional molecular changes within the monolayer phases during compression (difficult to imagine). This shows that the film at least contains coherent parts.

In contrast, coherent superposition of the density profiles for the pure phases according to Eq. 3 (index $1 = a$, $2 = e$) with adjusted area fractions gives a semiquantitative agreement with the density profiles *b* to *d*. The deduced reflectograms are still better than those obtained with incoherent superposition.

Molecularly spoken, between *b* and *e* a transition between an expanded and condensed phase might occur on a submicrometer scale, which is supported by the observation of a very broad domain size distribution ~ 5 μm in the fluorescence images *A* and *B*. The fits of *b* to *e* with a coherent domain model described in the Appendix show a decreasing area fraction α of the fluid phase in the film from 86 to 12%. In this model a series of assumptions were made, therefore the molecular parameters (cf. Fig. 5) are different from those obtained from calculating the extrema separation in $d\rho/dz$ (Fig. 4 *b*). The 18.6 Å found in GID as thickness of the ordered chains is somewhat below the values extracted from the reflectivity (22.4 and 23.8 Å, according to the different models), probably reflectivity attributes the double bound and the NH-groups to the chain region. Also, the main conclusions concerning chain stretching in the ordered phase and small headgroup change are the same. The advantage of this model is that one obtains some quantitative information on the headgroup electron density. The electron density in the chain slab increases from 0.29 to 0.31 electrons/$Å^3$ for the chain layer and from 0.40 to 0.52 electrons/$Å^3$ for the headgroup layer. The change of ρ_h is higher in the condensed phase, where it is similar to that of a dehydrated sugar crystal. Last but not least, the distribution of chain lengths is seen as an increased roughness at the chain/air interface.

We find that the condensed molecules grow into the water subphase rather than into the air as many models suggest (Möhwald et al., 1995). The alternative model for a domain growth into the air was checked with a variation on the domain model. An offset ($\approx$10 Å) was introduced to shift the density profiles *a* to *c* in such a way that all headgroups are aligned. But this model leads to contradictions. First, in all fits the electron density of the chain layer is low ($<$0.30 electrons/$Å^3$), which is inconsistent with ordered chains. Second, curve *c* could not be fitted with this model.

As an alternative, a laterally homogeneous three-slab model was tried for curves *b* to *e*. Taking into account that the box-model laterally averages over the electron density within the film, the slabs represent the top chain layer, an intermediate layer containing lipid chains as well as headgroups, and finally a water layer containing headgroups. The consequence is that the middle slab shows an electron density between that of chains and headgroups. The water adjacent slab exhibits an electron density which exceeds the one of water, and, on compression, the water adjacent slab becomes the one with the highest electron density because the headgroup concentration continuously increases. Simultaneously, the electron density of the middle slab *decreases* with compression because more and more molecules move toward the subphase, thus *depleting* the middle slab of headgroups. The air-adjacent slab can molecularly be found in the longer disordered chain ends raising over the shorter-ordered chains in HFA. It might account for an additional structural roughness at the film surface found in the domain model (5.0 Å instead of 3.9 Å). These details of the three-slab model are in excellent agreement with the coherent domain model, describing growth of HFA molecules into the water subphase.

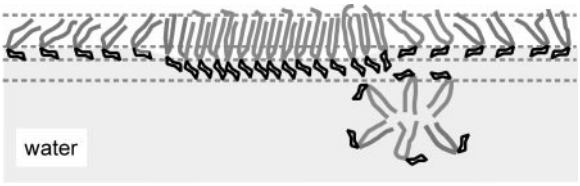

FIGURE 7 Molecular interpretation of the phase behavior of compressed HFA on pure water at 30°C. The monolayer is inhomogeneous with a higher-ordered phase forming on a micrometer scale. The micelles grow into the subphase rather than into the air.

Note that beside x-ray reflectivity coherent superposition, there is no physical method available to distinguish domain growth into the subphase from domain growth into the air. The offset between the domains (cf. Eq. 4) is a phase-shift, when the absolute of the Fourier transform of the respective profiles is calculated, thus it is experimentally accessible. For incoherent superposition occurring with larger domains or lower coherence lengths, the Fourier transform is calculated separately for each domain. Because Fourier transforms are invariant to phase-shifts, one can not measure the offset. In most cases, the optical methods are not sensitive enough to resolve details of the profile. The coherence length of neutrons would be long enough (mm); however, the available intensity is low and, thus, the accessible Q range limited. We find that during the chain-ordering transition, the chain/air interface is maintained, and the molecules grow into the water phase. We do not know how general that finding is, yet suspect that it is rather special for the HFA.

To calculate the line tension of a domain, one multiplies the thickness difference between the two coexisting phases with the interfacial energy of the protruding domain border. The main experimental evidence for this definition is the decrease of the line tension on temperature increase (manifested in a lower nucleation barrier at the fluid/ordered-phase transition), which is attributed to the experimentally found decreased thickness difference (Helm and Möhwald, 1988) between the phases, not on the physical composition of the line edges. For phospholipids, it was suggested to take the hydrophobic/air interfacial energy (25–30 mJ/m^2) and multiply it with 6- to 2-Å thickness difference between fluid- and ordered-phase (Benvegnu and McConnell, 1993; Israelachvili, 1994). However, that interfacial energy is only a factor two smaller than the hydrophobic/water interfacial energy (50 mJ/m^2). If the large energy of a hydrophobic surface in water is reduced by the interaction with the sugar headgroups, a growth into the water can be imagined. Furthermore, the domain rim does not need to be abrupt (especially for HFA with the mixed chain lengths), but may be stretched over a few molecules. In that case cooperative effects definitely complicate and possibly change the picture (cf. Fig. 7). Additionally, the HFA headgroup is capable of multiple hydrogen bonds with water molecules and with neighboring molecules; this capability provides the possibility of different molecular alignments.

The monolayer destabilization is not a macroscopic process, as, for instance, is the folding of centimeter-sized monolayer sheets as found for lung surfactant (Lipp et al., 1998). Apparently, only a few molecules protrude into the water and form a monolayer adjacent micelle or bilayer fragment (because we do not observe the destabilization, the destabilizing spot has to be <1 μm, maximum). The isotherms are reversible and the dissolved HFA molecules reenter the monolayer; therefore, they have to be closely associated to the compressed monolayer. (If they would dissolve and achieve homogenous distribution in the subphase, they would never reenter). If molecules slide from the monolayer into the water, their chains are, at least temporarily, exposed to the headgroups and to the water. Apparently, the sugar groups are flexible, and do not disturb the chain lattice as much as the phospholipid headgroups do. Furthermore, the sugar groups decrease the hydrophobic/water energy, because they have many hydroxyl groups, extensive hydrogen bonding. These unusual headgroup properties may not only cause a counterintuitive domain growth, but also provide a pathway for the destabilization.

CONCLUSION AND OUTLOOK

The following molecular picture of HFA at the air-water interface emerges. In the expanded state, the HFA film exhibits a phase with disordered chains which consist of a homogeneous hydrophilic and hydrophobic moiety, described in x-ray reflectivity by two electron density slabs. Upon compression, an additional phase with tilted chains ordered in a monoclinic lattice grows into the subphase, possibly with a reoriented headgroup. The domains are small and their size is widely distributed. Further compression finally leads to a film with ordered chains and decreasing tilt angle (Fig. 7). The longer acyl chains protrude from the hydrocarbon chain lattice and increase the roughness of the chain/air interface. Simultaneously, in the condensed phase, disordered micelles rather than ordered multilayers grow into the subphase, leading to a reversible partial loss of molecules away from the interface.

Our findings indicate an unusual structure for GalC and support a key role for their proper function in myelin. In contrast to other lipids in myelin (e.g., phospholipids), the weakly interacting sugar headgroups allow for pronounced protrusions of the monolayer when compressed, accompanied by pronounced headgroup dehydration. This layer flexibility appears to be meaningful to achieve additional stability in myelin by offering polarity to an apposed binding surface such as another bilayer within the myelin sheath or a protein. The hydroxyl groups thereby might offer multiple binding sites for complexation with ions or hydrogen bonds to the binding partners. The small headgroup influence leads to a high compressibility of the hydrophobic lipid

chains, smoothly counteracted by the dehydration, rendering the membrane less permeable, e.g., for ions, and thus to better isolation of the axons than, for example, phospholipids with dominating headgroups.

The authors thank Centaur Pharmaceuticals Inc. (Sunnyvale, CA), the University of California, and the National Multiple Sclerosis Society (RG 2795-A-3) for supporting parts of this work. We are grateful to Jim Joseph of the USDA Human Nutrition Research Center on Aging at Tufts University for providing the NIMA 622 Langmuir trough and associated equipment.

Discussions with Helmuth Möhwald and Gerald Brezesinski are appreciated. Kristian Kjaer is thanked for his support with the spectrometer at BW1 (Hasylab, DESY, Hamburg, Germany). Ute Kolb's help in simulating different molecular conformations of HFA with the simulation program Cerius on the base of crystal data from literature facilitated the interpretation of the molecular parameters a lot. The hospitality of Manfred Schmidt and Hans-Jürgen Butt is gratefully acknowledged. The financial support of the Schwerpunkt Benetzung (He 1616/9–3) and the SFB 262 was helpful.

APPENDIX

The fits to the reflectograms in Fig. 3 were carried out as described here: curve *a* was modeled with two slabs. These constraints were used: same roughness σ for all interfaces, and the thickness of the headgroup layer was set to 2σ. This gives four free parameters, thickness of the chain slab, two electron densities, and the roughness (the thickness of the water adjacent layer was in the range of twice the roughness thus leading to an unstable fit).

The reflectivity curves *b* to *e* were modeled with a coherent two-domain model with two slabs for each domain. The headgroup is the same in both domains, both thickness and electron density. The chain electron density is the same for both domains, too. Varied are the roughness, the area fraction, the headgroup thickness and density, the chain density, and the respective chain lengths (seven free parameters). To get physically reasonable values, parameters were set constant: In *d* and *e* the electron density of the chain layer was set to 0.29 and 0.31 electrons/Å^3, respectively, after checking the range from 0.28 to 0.33 electrons/Å^3. Moreover, in *b* and *e* the thickness of the water-adjacent layer was set to 7 and 7.6 Å, respectively, to avoid the divergence after trial fits in the range of 5–9 Å. It was necessary to introduce a large additional roughness (5 Å) at the chain/air interface in curve *e*. Here, we assumed a lower second roughness of 3.9 Å at the chain/headgroup interface. The thus-derived set of parameters is shown in Fig. 5.

REFERENCES

Ahrens, H., N. Hugenberg, M. Schmidt, and C. A. Helm. 1999. Wetting of mesoscopic soft cylinders: structure and layering transitions. *Phys. Rev. E.* 60:4360–4370.

Alberts, B., D. Bray, J. Lewis, M. Raff, K. Roberts, and J. D. Watson. 1983. Molecular biology of the cell. Garland Publishing, New York.

Albrecht, O., H. Gruler, and E. Sackmann. 1978. Polymorphism of phospholipid monolayers. *J. Phys.* 39:301–313.

Als-Nielsen, J. 1986. Solid and liquid surfaces studied by synchrotron x-ray diffraction. *In* Structure and Dynamics of Surfaces. W. Sommers and W. Blanckenhagen, editors. Springer, New York.

Als-Nielsen, J., and K. Kjaer. 1989. X-ray reflectivity and diffraction studies of liquid surfaces and surfactant monolayers. *In* Phase Transitions of Soft Condensed Matter. T. Riste and T. Sherrington, editors. Plenum Press, New York.113–137.

Asmussen, A., and H. Riegler. 1996. Numerical analysis of x-ray reflectivity data from organic thin films at interfaces. *J. Chem. Phys.* 104: 8159–8164.

Baltes, H., M. Schwendler, C. A. Helm, and H. Möhwald. 1996. Tail and headgroup interactions in phospholipid monolayers. *J. Colloid Interface Sci.* 178:135–143.

Benvegnu, D. J., and H. M. McConnell. 1993. Line tension between liquid domains in lipid monolayers. *J. Phys. Chem.* 97:6686–6691.

Boggs, J. M., A. Menikh, and G. Rangaraj. 2000. *Trans* interactions between galactosylceramide and cerebroside sulfate across apposed bilayers. *Biophys. J.* 78:874–885.

Bosio, A., H. Büssow, J. Adam, and W. Stoffel. 1998. Galactosphingolipids and axono-glial interaction in myelin of the central nervous system. *Cell Tissue Res.* 292:199–210.

Coetzee, T., K. Suzuki, and B. Popko. 1998. New perspectives on the function of myelin galactolipids. *Trends Neurosci.* 21:126–130.

Curatolo, W. 1986. The interactions of 1-palmitoyl-2-oleylphosphatidylcholine and bovine brain cerebroside. *Biochim. Biophys. Acta.* 861: 373–376.

Ding, J. Q., D. Y. Takamoto, A. v. Nahmen, M. M. Lipp, K. Y. Lee, A. J. Waring, and J. A. Zasadzinski. 2001. Effects of lung surfactant proteins, SP-B and SP-C, and palmitic acid on monolayer stability. *Biophys. J.* 80:2262–2272.

Dyer, C. A., and J. A. Benjamins. 1990. Glycolipids and transmembranes signaling: antibodies to galactocerebroside cause an influx of calcium in oligodendrocytes. *J. Cell Biol.* 111:625–633.

Dyer, C. A., and J. A. Benjamins. 1991. Galactocerebroside and sulfatide independently mediate Ca^{2+} responses in oligodendrocytes. *J. Neurosci. Res.* 30:699–711.

Genain, C. P., B. Cannella, S. L. Hauser, and C. S. Raine. 1999. Identification of autoantibodies associated with myelin damage in multiple sclerosis. *Nature Med.* 5:170–175.

Helm, C. A., and H. Möhwald. 1988. Equilibrium and nonequilibrium features determining superlattices in phospholipid monolayers. *J. Phys. Chem.* 92:1262–1266.

Helm, C. A., H. Möhwald, K. Kjaer, and J. Als-Nielsen. 1987a. Phospholipid monolayer density distribution perpendicular to the water surface. A synchrotron x-ray reflection study. *Eur. Phys. Lett.* 4:697–703.

Helm, C. A., H. Möhwald, K. Kjaer, and J. Als-Nielsen. 1987b. Phospholipid monolayers between fluid and solid states. *Biophys. J.* 52:381–391.

Helm, C. A., P. Tippmann-Krayer, H. Möhwald, J. Als-Nielsen, and K. Kjaer. 1991. The phases of phosphatidyl ethanolamine monolayers studied by synchrotron x-ray scattering. *Biophys. J.* 60:1457–1476.

Ibn-Elhaj, M., H. Riegler, H. Möhwald, M. Schwendler, and C. A. Helm. 1997. X-ray reflectivity study of layering transitions and the internal multilayer structure of films of liquid-crystalline three-block amphiphilic smectogens at the air/water interface. *Phys. Rev. E.* 56:1844–1852.

Israelachvili, J. 1994. Self-assembly in two dimensions: surface micelles and domain formation in monolayers. *Langmuir.* 10:3774–3781.

Johnston, D. S., and D. Chapman. 1988. The properties of brain galactocerebroside monolayers. *Biochim. Biophys. Acta.* 937:10–22.

Kaganer, V. M., H. Möhwald, and P. Dutta. 1999. Structure and phase transitions in Langmuir monolayers. *Rev. Mod. Phys.* 71:779–819.

Kenn, R. M., C. Böhm, A. M. Bibo, I. R. Peterson, H. Möhwald, J. Als-Nielsen, and K. Kjaer. 1991. Mesophases and crystalline phases in fatty acid monolayers. *J. Phys. Chem.* 95:2092–2097.

Kjaer, K., J. Als-Nielsen, C. A. Helm, L. A. Laxhuber, and H. Möhwald. 1987. Ordering in lipid monolayers studied by synchrotron x-ray diffraction and fluorescence microscopy. *Phys. Rev. Lett.* 58:2224–2227.

Koshy, K. M., J. Wang, and J. M. Boggs. 1999. Divalent cation-mediated interaction between cerebroside sulfate and cerebrosides: an investigation of the effect of structural variations of lipids by electrospray ionization mass spectrometry. *Biophys. J.* 77:306–318.

Lee, D. C., I. R. Miller, and D. Chapman. 1986. An infrared spectroscopic study of metastable and stable forms of hydrated cerebroside bilayers. *Biochim. Biophys. Acta.* 859:266–270.

Lipp, M. M., K. Y. Lee, D. Y. Takamoto, J. A. Zasadzinski, and A. J. Waring. 1998. Coexistence of buckled and flat monolayers. *Phys. Rev. Lett.* 81:1650–1653.

Lipp, M. M., K. Y. Lee, A. Waring, and J. A. Zasadzinski. 1997. Fluorescence, polarized fluorescence, and Brewster angle microscopy of palmitic acid and lung surfactant protein B monolayers. *Biophys. J.* 72:2783–2804.

Miller, A., and H. Möhwald. 1987. Diffusion limited growth of crystalline domains in phospholipid monolayers. *J. Chem. Phys.* 86:4258–4265.

Möhwald, H., H. Baltes, M. Schwendler, C. A. Helm, and H. Haas. 1995. Phospholipid and protein monolayers. *Jpn. J. Appl. Phys.* 34: 3906–3913.

Nelson, D. R., and B. I. Halperin. 1979. The hexatic phase. *Phys. Rev. B.* 19:2457–2484.

Ohler, B., I. Revenko, and C. Husted. 2001. Atomic force microscopy of nonhydroxy galactocerebroside nanotubes and their self-assembly at the air-water interface, with applications to myelin. *J. Struct. Biol.* 133:1–9.

Parratt, L. G. 1954. Surface studies of solids by total reflection of x-rays. *Phys. Rev.* 95:359.

Pascher, I., and S. Sundell. 1977. Molecular arrangements in sphingolipids. The crystal structure of cerebroside. *Chem. Phys. Lipids.* 20:175–191.

Pedersen, J. S. 1992. Model-independent determination of surface scattering-length-density profile from specular reflectivity data. *J. Appl. Crystallogr.* 25:129–145.

Pedersen, J. S., and I. W. Hamley. 1994. Analysis of neutron and x-ray reflectivity data. II. Constrained least-square methods. *J. Appl. Crystallogr.* 27:36–49.

Pershan, P. S. 1994. The effect of surface profile and interface correlations on x-ray reflectivity from fluid interfaces. *J. Phys. Condens. Matter.* 6:A37–A50.

Pincet, F., T. L. Bouar, Y. Zhang, J. Esnault, J. M. Mallet, E. Perez, and P. Sinay. 2001. Ultraweak sugar-sugar interactions for transient cell adhesion. *Biophys. J.* 80:1354–1358.

Ries, H. E. 1982. Heart-shaped monolayer islands and ridged collapse structures of ceramide galactocerebroside. *J. Colloid Interface Sci.* 88:298–301.

Salditt, T., H. Rhan, T. H. Metzger, J. Peisl, R. Schuster, and J. P. Kotthaus. 1994. X-ray coherence and ultra-small angle resolution at grazing-incidence and exit angles. *Zeitschrift Phys. B. Condens. Matter.* 96:227–230.

Sastry, P. S. 1985. Lipids of nervous tissue: composition and metabolism. *Prog. Lipid Res.* 24:69–176.

Simons, K., and E. Ikonen. 1997. Functional rafts in cell membranes. *Nature.* 387:569–572.

Stryer, L. 1988. Biochemistry. W. H. Freeman and Company, New York.